Synthesis and electronic properties of $Nd_{n+1}Ni_nO_{3n+1}$ Ruddlesden-Popper nickelate thin films

Grace A. Pan , Qi Song, Dan Ferenc Segedin, Myung-Chul Jung, Hesham El-Sherif, Erin E. Fleck, Berit H. Goodge , 4,5 Spencer Doyle, Denisse Córdova Carrizales, Alpha T. N'Diaye, Padraic Shafer, Hanjong Paik , Lena F. Kourkoutis , 4,5 Ismail El Baggari, Antia S. Botana , Charles M. Brooks, and Julia A. Mundy Lena F. Kourkoutis , 4,5 Ismail El Baggari, Antia S. Botana , Charles M. Brooks, and Julia A. Mundy Lena F. Kourkoutis , 4,5 Ismail El Baggari, Antia S. Botana , Charles M. Brooks, and Julia A. Mundy , Department of Physics, Harvard University, Cambridge, Massachusetts, USA

Department of Physics, Arizona State University (ASU), Tempe, Arizona, USA

The Rowland Institute, Harvard University, Cambridge, Massachusetts, USA

Skavli Institute at Cornell for Nanoscale Science, Cornell University, Ithaca, New York, USA

Kavli Institute at Cornell for Nanoscale Science, Cornell University, Ithaca, New York, USA

Platform for the Accelerated Realization, Analysis and Discovery of Interface Materials (PARADIM), Cornell University, Ithaca, New York, USA

(Received 31 October 2021; accepted 11 April 2022; published 16 May 2022)

The rare-earth nickelates possess a diverse set of collective phenomena including metal-to-insulator transitions, magnetic phase transitions, and upon chemical reduction, superconductivity. Here, we demonstrate epitaxial stabilization of layered nickelates in the Ruddlesden-Popper form $Nd_{n+1}Ni_nO_{3n+1}$ using molecular beam epitaxy. By optimizing the stoichiometry of the parent perovskite $NdNiO_3$, we can reproducibly synthesize the n=1-5 member compounds. X-ray absorption spectroscopy at the O K and Ni L edges indicate systematic changes in both the nickel-oxygen hybridization level and nominal nickel filling from $3d^8$ to $3d^7$ as we move across the series from n=1 to ∞ . The n=3-5 compounds exhibit weakly hysteretic metal-to-insulator transitions with transition temperatures that depress with increasing order toward $NdNiO_3$ ($n=\infty$).

DOI: 10.1103/PhysRevMaterials.6.055003

I. INTRODUCTION

The perovskite rare-earth nickelates $RNiO_3$ (R = La, Pr, Nd...) are strongly correlated materials with a rich, tunable phase diagram that includes features such as metalto-insulator transitions and noncollinear antiferromagnetism [1,2]. The Ruddlesden-Popper nickelates, represented by the chemical formula $R_{n+1}Ni_nO_{3n+1}$, are the layered analogues of the perovskite rare-earth nickelates. Also expressed as $(RNiO_3)_n(RO)$, these compounds comprise n layers of the traditional perovskite motif RNiO₃ separated by rock salt spacer layers R-O, as shown in Fig. 1(a). The R-O layer tunes the dimensionality of the system from the three-dimensional $RNiO_3$ $(n = \infty)$ to the quasi-two-dimensional R_2NiO_4 $(n = \infty)$ 1). The phenomenology of the R_2NiO_4 family of compounds is distinct from its perovskite counterparts: for example, while the perovskite LaNiO₃ is a strongly correlated metal [1,3,4], single-layer La₂NiO₄ displays insulating charge and spin stripes, with a spatial modulation tunable with doping [5,6]. Accordingly, the evolution of the charge and spin structure with perovskite layer thickness (or order) n in the Ruddlesden-Popper nickelates has been of sustained interest, especially as many of these ordered phases precede superconductivity in the cuprates [7]. Indeed, the Ruddlesden-Popper nickelates have long been viewed as close cousins of the cuprates [8–10], and it was recently found that the $n = 5, \infty$ compounds exhibits superconductivity when chemically reduced into the square-planar form [11,12].

Despite longstanding interest, synthesis of the Ruddlesden-Popper nickelates remains a key challenge. Early studies on the n = 2, 3 member compounds in powder form identified analogies to the superconducting cuprates including a putatively similar band structure and possible charge density wave (CDW) transitions [8,13-15]. More recently, advances in the preparation of large single-crystal specimens [10,16] have enabled direct study of these features which were originally proposed from powder specimen behavior [17,18]. Nevertheless, the higher-order compounds $(n \ge 4)$, which are of particular interest as the n = 5 becomes superconducting when reduced [12], remain inaccessible using powder or single-crystal synthetic methods [16]. Instead, these compounds require atomic layering control. In addition to the synthesis of the superconducting n = 5 square-planar compound with molecular beam epitaxy (MBE), the stabilization of the $La_{n+1}Ni_nO_{3n+1}$ [19] and $Nd_{n+1}Ni_nO_{3n+1}$ [20] series for n = 1-5 also using MBE has recently been reported. Atomically precise thin film deposition thus allows access to the $R_{n+1}Ni_nO_{3n+1}$ series beyond n=3.

In this paper, we describe a generalizable synthetic strategy for thin film Ruddlesden-Popper nickelates $Nd_{n+1}Ni_nO_{3n+1}$ (n=1-5), using MBE. By first optimizing the crystalline growth of the perovskite $NdNiO_3$ on $LaAlO_3$ substrates, we can reproducibly stabilize the higher-order layered Ruddlesden-Popper nickelates. From x-ray absorption spectra (XAS), we observe that tuning the layering n of the Ruddlesden-Popper nickelates changes the nickel electronic

^{*}mundy@fas.harvard.edu

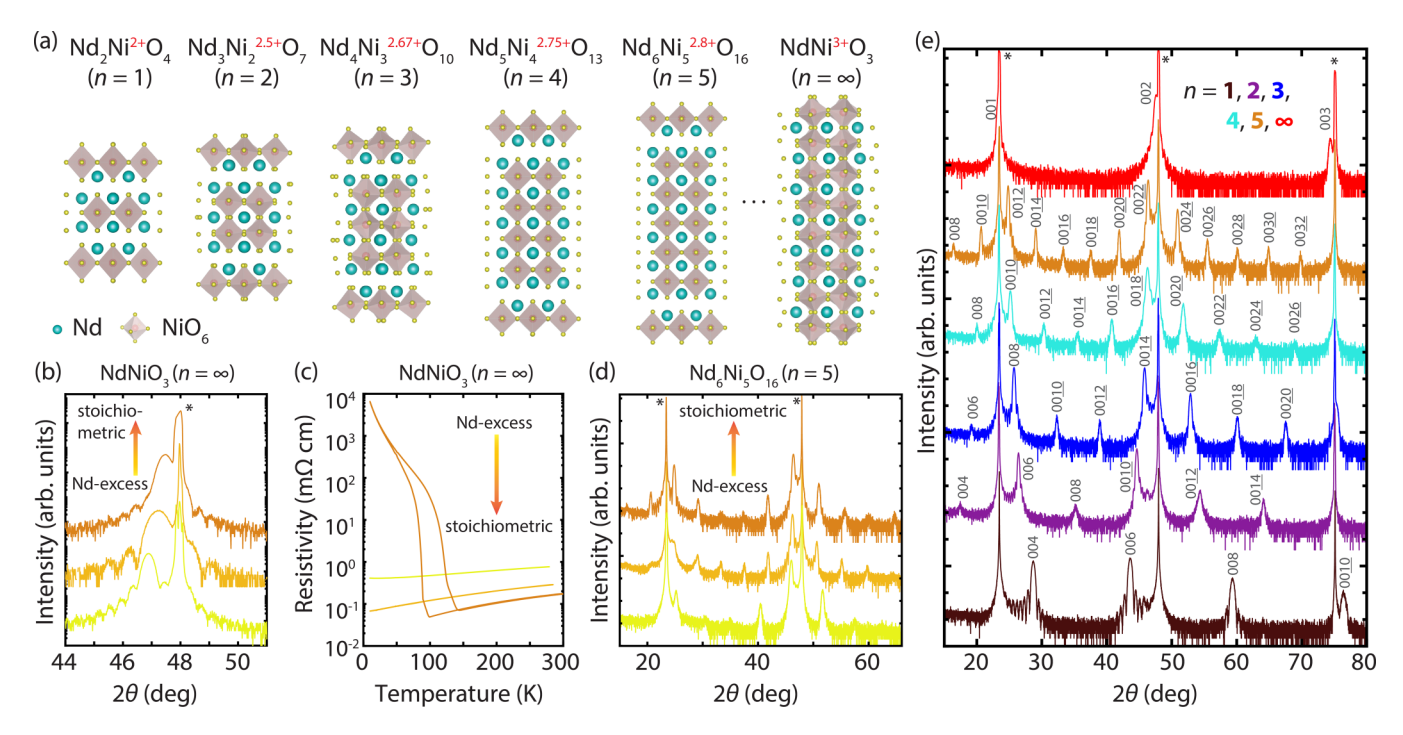


FIG. 1. Structural description and characterization of the Ruddlesden-Popper $Nd_{n+1}Ni_nO_{3n+1}$ compounds. (a) Crystal structures of the $Nd_{n+1}Ni_nO_{3n+1}$. Nd, Ni, and O in turquoise, red, and yellow, respectively. The n=4 and n=5 are drawn without octahedral rotations as there is no existing crystallographic data. (b) X-ray diffraction (XRD) spectra and (c) electrical resistivity characterization of two separate parent perovskite $NdNiO_3$ calibrations that were used to synthesize the two n=5 compounds in (d). Although both $NdNiO_3$ films are phase pure and show sub-nanometer surface roughness, using the calibration from an off-stoichiometric calibration forms a higher-order Ruddlesden-Popper of reduced crystallinity. (e) XRD spectra of all the $Nd_{n+1}Ni_nO_{3n+1}$ (n=1-5) synthesized with optimized $NdNiO_3$ calibrations. Asterisks denote substrate peaks.

filling and relative transition-metal-oxygen hybridization levels, as would be expected from electron counting rules. Furthermore, there are systematic changes in the x-ray linear dichroism (XLD) which we attribute to energy level splittings in the e_g orbitals. In the electronic transport, we observe in the $n \ge 2$ compounds metal-to-insulator transitions with features that interpolate between those of the parent perovskite NdNiO₃ and bulk crystal specimens of Nd_{n+1}Ni_nO_{3n+1} (n = 3) [8].

II. EXPERIMENTAL METHODS

A. Synthesis via MBE

We use ozone-assisted MBE to synthesize the Ruddlesden-Popper nickelates in the thin film form. The evolution of the nickel valence from Ni^{2+} in the Nd_2NiO_4 (n = 1) compound to Ni³⁺ in the NdNiO₃ compound necessitates varied synthetic conditions [16]—as hot as 1000 °C for Nd₂NiO₄ and as cold as 550 °C for NdNiO₃. We synthesize the Nd₂NiO₄ (n = 1) compound using the simultaneous evaporation of both elements (hereafter, codeposition) at high (~900–1000 °C) temperatures with fluxes estimated using a quartz crystal microbalance with applied tooling factors. We also note that it is possible to synthesize the n = 2, 3 and perovskite layer compounds using the codeposition method by tuning only the relative flux ratios, temperature, and oxidation pressure, like what has been done for single crystals [16]. On the other hand, the $n \ge 4$ compounds, which have not been synthesized as bulk crystals, also cannot be synthesized with codeposition. These compounds therefore require the precise sequential deposition of the neodymium and nickel sources, wherein a single monolayer of each element is deposited at a time, to achieve the Ruddlesden-Popper layering.

In principle, MBE enables one to precisely control the monolayer deposition times and hence synthesize a generic Ruddlesden-Popper compound of arbitrary order n. There are key differences, however, between the Ruddlesden-Popper nickelates and other Ruddlesden-Popper systems such as the more commonly studied $Sr_{n+1}Ti_nO_{3n+1}$ which make the direct translation of other synthetic calibration techniques onto the nickelates difficult. In $Sr_{n+1}Ti_nO_{3n+1}$ compounds, deviations from perfect stoichiometry by as much as 5+% often result in imperfect superlattices with rock salt intergrowths or missing rock salt layers but without substantial phase segregation [21,22]. Errors in monolayer dosing times can then be quantitatively estimated and adjusted for purely based on x-ray diffraction (XRD) spectra of the superlattice phase [23]. The composition, or A : B cation ratio in an ABO_3 compound, can also be perfected using quantitative analysis of the beat frequencies and oscillation lineshapes in the reflection highenergy electron diffraction (RHEED) intensities [22,24].

In contrast, a principal challenge in nickelate thin film synthesis is the stabilization of the high oxidation Ni³⁺ state. Insufficient oxidizing conditions can promote the phase segregation of Ni²⁺ compounds such as polycrystalline NiO [9,25]. The presence of NiO, however, can result not only from insufficient oxidation but also from errors in composition or monolayer dosing and most frequently from a combination of

all three. This propensity to phase segregate makes assessing quantitative changes to monolayer dosing challenging. Moreover, it is difficult to use RHEED oscillations to precisely adjust for composition errors: once a secondary phase such as NiO forms, RHEED oscillation intensities fade and do not recover, whereas oscillations can persist for much longer in SrTiO₃-based compounds [22,24].

To address these challenges, we have developed an alternative calibration method that reliably facilitates the synthesis of $n \ge 2$ Ruddlesden-Popper $Nd_{n+1}Ni_nO_{3n+1}$ compounds. This method optimizes the synthesis of the parent perovskite NdNiO₃: by iteratively improving both its stoichiometric composition and monolayer dose estimates, we can obtain precise shuttering times to synthesize the higher-order Ruddlesden-Popper compounds with atomistic precision. We start by adjusting the temperature of the neodymium and nickel effusion cells to read $\sim 1 \times 10^{13}$ atoms cm⁻¹ s⁻¹ on a quartz crystal microbalance. We then synthesize the binary oxides Nd₂O₃ on Y: ZrO₂ (111) and NiO on MgO (100) and use x-ray reflectivity (XRR) to estimate the film thicknesses and thus the actual effusion cell fluxes [26]. These estimates give us approximate values of the neodymium and nickel fluxes, which we then fine-tune with the synthesis of

From the rough flux estimates provided by the binary oxide compounds, we perform the shuttered growth of NdNiO₃. In our initial calibration scheme, we intentionally deposit <1 full monolayer of both neodymium and nickel. The accidental deposition of > 1 full monolayer can exacerbate the formation of polycrystalline NiO phases, which would be observed in the RHEED (Fig. S4 of the Supplemental Material [27]), even if the elements are supplied in a one-to-one composition ratio. Hence, in this underdosed regime, we can focus on tuning the composition ratio of neodymium and nickel. Like other oxide perovskites [22], the parent compound NdNiO₃ is capable of accommodating some A-site (neodymium) excess into the lattice, while still forming a single-phase film, as ascertained by RHEED and atomic force microscopy (AFM). This A-site excess is manifest as an expansion of the out-of-plane lattice constant as well as in a broadening or even suppression of the metal-to-insulator transition [28,29]. By tracking the evolution of the lattice constants for a range of Nd: Ni ratios, we have found that an optimally stoichiometric NdNiO3 film on LaAlO₃ possesses a lattice constant of \sim 3.82 Å, corresponding to a (002) film peak that nearly coincides with that of the substrate LaAlO₃ [28,29]. The metal-to-insulator transition in these stoichiometric films spans as much as over five orders of magnitude; films with excess neodymium have a higher room temperature resistivity and may possess an entirely suppressed metal-to-insulator transition. We note that it is also possible to form a nickel-rich NdNiO₃ phase [25], though we have found that nickel excess will more frequently appear as a secondary NiO phase in situ in the RHEED pattern (Fig. S4 in the Supplemental Material [27]). After fine-tuning this shuttered stoichiometric calibration in the underdosed regime, we then correct for the monolayer dosing using thickness estimates from XRR fits to the NdNiO₃ films. Finally, we apply the monolayer deposition times from the calibrated NdNiO₃ to synthesize the Ruddlesden-Popper compounds. We synthesize the $Nd_{n+1}Ni_nO_{3n+1}$ ($n \ge 2$) compounds at a substrate temperature of 630–690 °C as verified by an optical pyrometer and using distilled ozone in chamber pressures of 1.2×10^{-6} to 2.0×10^{-6} Torr.

Figures 1(b)-1(d) illustrate this approach using three different calibrations from NdNiO3 films. The stoichiometric film possesses a lattice constant of 3.82(7) Å; in contrast, the A-site-rich films have expanded lattice constants of 3.84(5) and 3.87(3) Å, corresponding to neodymium in excess of \sim 3 and $\sim 10\%$, respectively, estimated from our neodymium flux calibrations [Fig. 1(b)]. Importantly, we note that this A-site excess is not always manifest in surface-sensitive characterizations such as RHEED or AFM (Fig. S4 in the Supplemental Material [27]) images, which show that the A-site excess films are ostensibly high quality. Hence, we confirm the superior quality of the stoichiometric film using resistivity measurements which present a sharp metal-to-insulator transition in Fig. 1(c). Finally, using the three different shuttered calibrations from these three NdNiO3 films, we synthesize the $Nd_6Ni_5O_{16}$ (n = 5) compound. As shown in the XRD spectra in Fig. 1(d), the Nd₆Ni₅O₁₆ synthesized from the two A-site excess films display predominant Ruddlesden-Popper layering but with weaker superlattice ordering. The Nd₆Ni₅O₁₆ film synthesized from the least stoichiometric NdNiO3 calibration possesses superlattice peaks approaching those of an n = 4 compound, and neither film exhibits sharp lower-order peaks. In contrast, the Nd₆Ni₅O₁₆ film synthesized from the stoichiometric $NdNiO_3$ calibration displays coherent n = 5ordering with the full emergence of the lower-order (0010) and (0012) superlattice peaks, which are sensitive to the longrange order of the film. This indicates the sensitivity of the Ruddlesden-Popper nickelates to composition, requiring a calibration procedure that enables fine tuning.

B. Structural characterization

Thin film XRD spectra were taken on a Malvern Panalytical Empyrean diffractometer using Cu K α_1 ($\lambda = 1.5406$ Å) radiation. Reciprocal space maps (RSMs) were taken on the same instrument using a PIXcel3D 2D pixel area detector. Cross-section scanning transmission electron microscopy (STEM) specimens were prepared using an FEI Helios focused-ion beam with a gallium ion source. The final thinning step was performed using 2 keV gallium ions. Atomic-resolution STEM imaging was performed using a Thermo Fisher Scientific Themis Z G3 transmission electron microscope operated at 200 keV with probe convergence angle of ~19.6 mrad and an annular dark-field (ADF) collection angle range of ~78-200 mrad. Additional STEM imaging was performed on an aberration-corrected JEOL ARM 200F transmission electron microscope at 200 keV with a probe convergence angle of ~22 mrad and an ADF collection angle range of \sim 68–220 mrad. The displayed images were obtained from the average of 20 cross-correlated frames each acquired with 500 nS dwell time.

To map the local distortions of specific lattice fringes, we performed a phase lock-in analysis on the high-angle ADF-STEM (HAADF-STEM) images. By taking the gradient of the local phase, we can generate a map of local strain along the c direction [30–32]. The strain map highlights Ruddlesden-Popper rock salt layers, which appear as regions of local

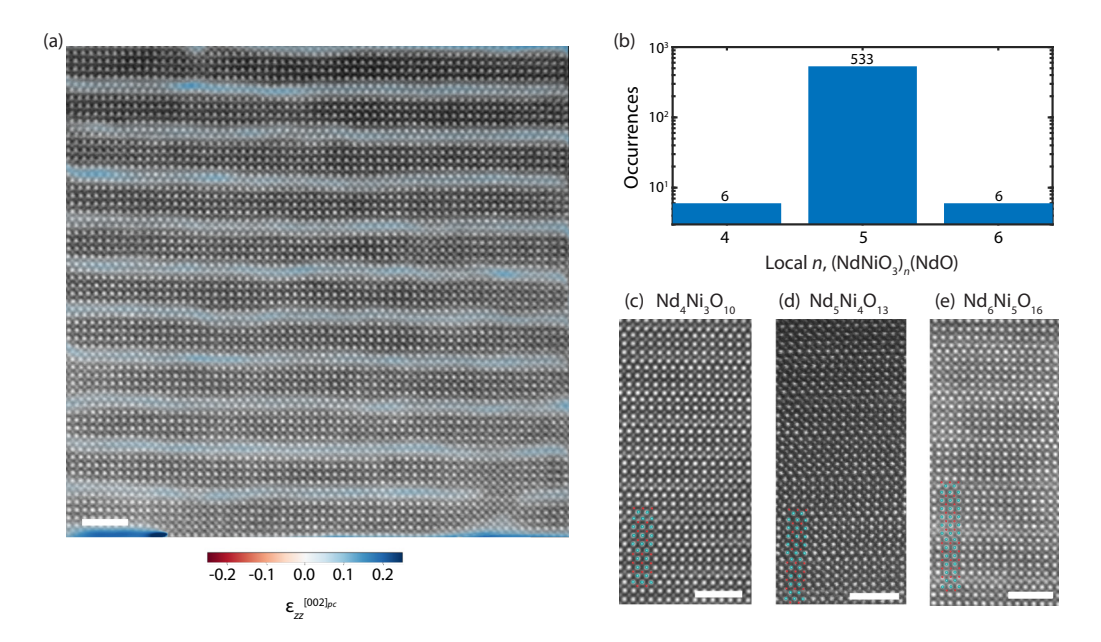


FIG. 2. High-angle annular dark-field scanning transmission electron microscopy (HAADF-STEM) images of Ruddlesden-Popper $Nd_{n+1}Ni_nO_{3n+1}$ compounds. (a) Large field of view of the $Nd_6Ni_5O_{16}$ (n=5) compound with an overlaid strain map to highlight the Ruddlesden-Popper layers. Scale bar, 2 nm. (b) Bar graph showing the number of occurrences of each of the Ruddlesden-Popper layers over the same field of view, plotted on a log scale. (c)–(e) High-resolution images of the (c) n=3, (d) n=4, and (e) n=5 compounds, illustrating the precise placement of the Nd-O rock salt double layers every n perovskite layers. Neodymium and nickel atoms are represented by turquoise and red, respectively. Scale bars, 2 nm.

tensile strain because the spacing between two adjacent Nd-O layers (\sim 2.7 Å) is greater than the spacing between the adjacent Nd-O and Ni-O layers (\sim 1.9 Å). Analyzing the strain profiles along the c-direction can thus be used to quantify distances between the rock salt spacer layers. This allows us to determine the locations and occurrences of local n layerings within a film, as demonstrated in Fig. 2. Further details on the phase lock-in analysis may be found in the Supplemental Material [27].

C. X-ray absorption spectroscopy

XAS were measured at the Advanced Light Source, Lawrence Berkeley National Lab, at Beamlines 4.0.2 and 6.3.1 in the total electron yield mode at 300 K. At Beamline 4.0.2, the spectra were acquired at 20° grazing incidence with linear horizontally (I_z) or vertically (I_x) polarized photons. At Beamline 6.3.1, the spectra were acquired exclusively with linear horizontally polarized incident photons but with the sample either normal (I_x) or at 30° grazing (I_z) to the beam. A geometric correction factor was applied for the grazing incident signal [33]. As energy calibrations can differ slightly between beamline endstations, we use $Nd-M_{4,5}$ features to align all Ni $L_{2,3}$ - and O K-edge spectra. All spectra are normalized to the incident x-ray flux, as monitored via the absorption by a semitransparent gold mesh upstream of the nickelate films. The spectra are further scaled so that the intensity is unity at energies slightly below the absorption edge and normalized across the entire edge. Each spectrum presented is polarization averaged $\left[\frac{1}{2}(I_x + I_z)\right]$ and represents the mean of 8–16 polarization-averaged scans. All x-ray linear dichroism (XLD) signals are given by $I_z - I_x$ ($\mathbf{E}||\mathbf{c} - \mathbf{E}||\mathbf{a}, \mathbf{b}$), the difference between spectra with photons polarized predominantly out-of-plane and in-plane with respect to the sample surface. The XLD spectra are normalized by the polarization-averaged integral $A = 2(I_x + I_z)/3$ [34].

D. Electrical transport

Electrical resistivities were determined using devices in van der Pauw or Hall bar geometries. Contacts comprising Cr (5 nm)/Au (100 nm) were deposited using an electron-beam evaporator and patterned with shadow masks. Hall bar channels were defined with a diamond scribe. Transport measurements down to 1.8 K were conducted in a Quantum Design Physical Property Measurement System equipped with a 9 T magnet using AC lock-in techniques at $\sim\!15$ Hz. Temperature-dependent Hall coefficients were calculated from linear fits of antisymmetrized field sweeps up to 9 T, all taken upon warming.

III. RESULTS AND DISCUSSION

A. Thin film growth

Using the growth calibration techniques described above, we present the XRD spectra of the fully epitaxially stabilized nickelate Ruddlesden-Poppers (n=1-5) on LaAlO₃ in Fig. 1(e). The XRD spectra display all the allowed even-numbered (00*l*) superlattice peaks. We extract the out-of-plane lattice constants from Nelson-Riley fits to the 2θ - θ spectra [35], tabulated in Table I.

To determine the in-plane lattice constants, we perform RSM on each of the films (see Fig. S2 in the Supplemental Material [27]). RSM scans indicate that the $n=2-5,\infty$ films are epitaxially strained to the LaAlO₃ substrate (a=3.79 Å), which provides $\varepsilon\approx-0.4\%$ strain to the bulk NdNiO₃ ($n=\infty$) and as much as $\varepsilon\approx-0.9\%$ strain

TABLE I. Nominal nickel valences (hypothetical) and structural parameters (experimental) for $Nd_{n+1}Ni_nO_{3n+1}$ epitaxially stabilized on LaAlO₃. A 2+ valence state is assumed for the n=1 compound.

Order	Hypothetical valence (filling)	Measured valence	c-axis lattice constant (Å)	Unit cell volume (ų)
$\overline{n=1}$	$2+(d^8)$	2+ (nominal)	12.450 ± 0.002	361 ± 0.06
n = 2	$2.5+(d^{7.5})$	2.5(7)+	20.20 ± 0.05	580 ± 1.5
n = 3	$2.67+(d^{7.33})$	2.6(7)+	27.728 ± 0.015	797 ± 0.43
n = 4	$2.75+(d^{7.25})$	2.7(9)+	35.35 ± 0.07	1016 ± 2
n = 5	$2.8 + (d^{7.2})$	2.8(4)+	43.12 ± 0.04	1239 ± 1.2

to the bulk $Nd_4Ni_3O_{10}$ (n = 3). However, our single-layer Nd_2NiO_4 (n = 1) film, which experiences a similar strain level of $\varepsilon \approx -0.9\%$, appears to have partially relaxed to an average $a \approx 3.81$ Å. This is still under the bulk lattice constant of $a_{\rm pc} = 3.825$ Å. This relaxation is likely order dependent; for example, in the single-layer Ruddlesden-Popper ruthenate Sr₂RuO₄, immediate relaxation has been reported on substrates providing $\varepsilon \gtrsim -0.9\%$ strain [36]. Indeed, while our Nd_2NiO_4 (n = 1) film exhibits partial relaxation as early as 17 nm, we could stabilize the Nd₄Ni₃O₁₀ (n = 3) to \sim 55 nm before we observed partial relaxation (see Fig. S3 in the Supplemental Material [27]). The films presented in Fig. 1(e) were all synthesized to have 60-75 nickel layers, resulting in thicknesses of 29.5, 27.7, 26.5, 32.4, and 22.9 nm for the n =2–5, ∞ compounds, respectively; meanwhile, the n=1 compound presented is 17 nm thick. With these in-plane lattice constants, we report the unit cell volumes in Table I. Compared with the bulk lattice constants of Nd₄Ni₃O₁₀ [13,16,37– 39], we observe a slight decrease in the overall unit cell volume by $\sim 0.7\%$ with the compressive epitaxial strain imposed by the LaAlO₃ substrate, as has also been observed in NdNiO₃ [40]. A more detailed discussion on the determination of lattice parameters and errors can be found in the Supplemental Material [27].

HAADF-STEM images taken across the series confirm the coherent layering at the microscopic level, as shown in Fig. 2. In Fig. 2(a), we observe a long-range coherent ordering of the horizontal Ruddlesden-Popper structure up to the total thickness of a 32-nm-thick n = 5 film, with no obvious vertical intergrowths observed within the largest fields of view of our imaging. In addition, atomic contrast provided by HAADF-STEM highlights the placement of the Nd-O rock salt layers every n unit cells of the perovskite motif, as exemplified in the close-up images in Figs. 2(c)–2(e) for the $n \ge 3$ compounds. We do, however, observe defect regions of reduced atomic contrast between the neodymium and nickel sites (Fig. S7 in the Supplemental Material [27]). We ascribe these to halfunit-cell offsets between regions of the film, likely caused by the occasional stacking fault, as opposed to the possibility of cation intermixing. Since STEM is a measurement in projection, these offsets would create regions where scattering intensities are averaged over both neodymium and nickel sites in the atomic columns.

In other Ruddlesden-Popper systems, areas of locally varying n are frequently observed [23,41–44]. To quantify the distribution of the Ruddlesden-Popper layerings, we employ phase lock-in analysis using the $(001)_{pc}$ and $(101)_{pc}$ peaks of the NdNiO₃ perovskite structure [30–32]. Figure 2(e) displays the strain map produced from the phase lock-in analysis,

we which we have superimposed on the bare STEM image. The map highlights Ruddlesden-Popper rock salt layers, which appear as regions of local tensile strain. We find that n=5 is indeed the dominant Ruddlesden-Popper layering for the nominal $Nd_6Ni_5O_{12}$ film presented in Figs. 1(e) and 2(b), though there are occasional occurrences of n=4 and 6 Ruddlesden-Popper layerings. A phase lock-in analysis is also sensitive to defect structures or anywhere there is a deviation from the periodicity corresponding to the Fourier peak, as illustrated in Fig. S7 in the Supplemental Material [27]. Additional details on the quantification of Ruddlesden-Popper layerings may be found in the Supplemental Material [27].

B. Electronic structure

To measure electronic structure changes across the Ruddlesden-Popper series, we use XAS. We start with the O K edges, which can provide a probe of the nickel valence. We focus on the prepeak, or first peak along the oxygen edge, which arises from the covalent mixing of the oxygen 2p with the nickel 3d states [45]. Due to varying contributions from the LaAlO₃ substrate \gtrsim 530 eV, we do not address the higher-energy fine structure features, whereas the lowerenergy prepeak region is free from background features. The full O K-edge spectra can be found in Fig. S8 in the Supplemental Material [27]. The intensity of this prepeak across members of a homologous transition metal series should scale with the number of unoccupied 3d states (increasing valence state) as per a 1s to hybridized 2p-3d (or $3d\underline{L}^n$ type transition) [45,46]. Here then, Nd₂NiO₄ with a nominal valence of Ni^{2+} should have the weakest intensity O K prepeak with a minor shift to higher energies representing transitions into states of the type $\alpha |3d^8\rangle + \beta |3d^9\underline{L}\rangle$ [47–49]. Meanwhile, NdNiO₃, with a valence of Ni³⁺ and a ground state dominated by highly covalent $3d^8\underline{L}^n$ states [50,51] (nominally $3d^7$), should have the strongest intensity prepeak, with all intermediate Ruddlesden-Poppers interpolating in between. Indeed, we observe this general trend in prepeak intensity across our $Nd_{n+1}Ni_nO_{3n+1}$ samples, as shown in Fig. 3(a). We quantify both the integrated prepeak intensities, which scale with the nickel-oxygen hybridization levels, and the maximum of the prepeak signal, which reflects the relative number of unoccupied states, as shown in Fig. S8 in the Supplemental Material [27]. In both quantities, and particularly in the estimates of the integrated prepeak intensities, the differences between the higher-order (n = 3-5) compounds are within error. This indicates that relative nickel-oxygen hybridization levels do not appreciably change between Ruddlesden-Popper compounds of increasing high order, unlike in their reduced square-planar

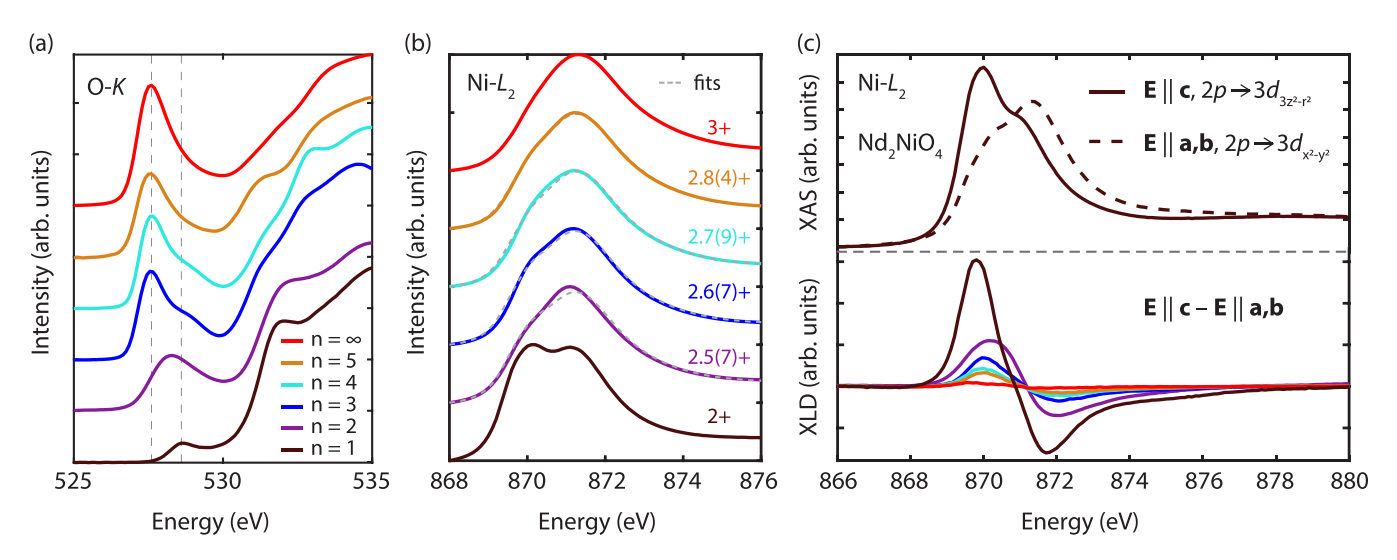


FIG. 3. X-ray absorption spectra (XAS) of the Ruddlesden-Popper $Nd_{n+1}Ni_nO_{3n+1}$ compounds. (a) Oxygen K-edge prepeak features. Dashed lines represent the spectral weights of transitions to the nominal $3d^7$ (left) and $3d^8$ (right) states. (b) Spectra across the Ni L_2 edge. Data are in solid curves. Fits to the data with nonnegative linear least squares fittings using the n=1 and ∞ spectra assigned as references are shown as dashed light gray curves. Estimated valences from the fits are shown on the side. (c) X-ray linear dichroic (XLD) signals (bottom) at the Ni L_2 edge, represented as E||c-E||a, b. An example of the polarization-dependent XAS signals used to determine the XLD from the n=1 compound is shown at the top.

counterparts [12]. Nevertheless, the general trend of increased prepeak intensity from n = 1 to ∞ points to an overall depletion of the nominal nickel 3d states and increasing covalency as we move down the Ruddlesden-Popper series from NdNiO₃ $(n = \infty)$ to Nd₂NiO₄ (n = 1).

To further assess the filling of the nickel 3d states, we can decompose this prepeak region into the two distinct features demarcated by the dotted gray lines in Fig. 3(a). We assign these features to represent transitions associated with the hybridized (nominal) $3d^7$ and $3d^8$ states [48,52]. Accordingly, the mixed-valence Ruddlesden-Poppers (n = 2-5) possess spectral weight from both these features with more of the lower-energy (higher-valence) feature as we increase the dimensionality of the system. This effect has been previously observed in single-layer $R_{2-x}Sr_xNiO_4$ compounds [47,48], where hole-doping away from Ni²⁺ toward Ni³⁺ shifts the total spectral weight of the O K prepeak toward lower-incident energy in XAS. With the recent observation of superconductivity in a layered nickelate [12] and the identification of inequivalent transition-metal planes in a five-layer cuprate [53], the layer-resolved distribution of the nickel valence is of increasing interest, though conflicting reports exist in bulk crystal studies [16,38]. This observation that the mixedvalence Ruddlesden-Popper compounds possess both Ni²⁺ and Ni^{3+} features in the O K-edge prepeak region, in contrast to previous work [54], provides a future means to use spatially resolved spectroscopic techniques such as electron-energy loss spectroscopy to identify any electronic modulation.

The Ni $L_{2,3}$ edges, which we present in Fig. 3(b), are comparatively more difficult to interpret due to core-hole effects [55] and are exquisitely sensitive to variations in the strain state, cation composition, and oxygen content [40,49,56,57]. The strong covalency effects in the oxidized nickelates complicate the quantitative extraction of valence, as can be performed in other perovskite oxides such as the

titanates or manganites [45,58,59]. Nevertheless, we can employ a self-consistent method to characterize the systematic evolution of the nickel valence across the series, as has been similarly performed using x-ray photoemission spectroscopy [20]. We define our spectra from the Nd_2NiO_4 (n = 1)and NdNiO₃ $(n = \infty)$ end-member compounds, which have been well characterized in the bulk [52,60], as proxies for the Ni²⁺ and Ni³⁺ reference spectra, respectively, within the layered nickelate series. We then use these reference spectra in a nonnegative linear least squares fitting to extract the nominal nickel valences as tabulated in Table I. As the octahedral coordination environments and transition metaloxygen hybridization should be reasonably similar across the Ruddlesden-Popper nickelates, we expect this approach to be more reflective of relative valence changes than using reference spectra from generic Ni²⁺ compounds such as NiO. The valences interpolate nearly monotonically between 2+ and 3+ as we move from n=1 to ∞ and are close to the expected values from simple electron counting rules. (Note that we employ this method on just the higher-energy Ni L_2 edges, which are free of the La M₄ background from the LaAlO₃ substrate that runs into the Ni L_3 edge, as seen in Fig. S8 in the Supplemental Material [27].) We attribute deviations from the ideal fractional valences to minor variations in cation stoichiometry and oxygen content which are challenging to quantify precisely in nickelate thin films. Nonetheless, this general procedure reveals the gradation of the nickel filling from formal $3d^8$ to $3d^7$ across the order of the Ruddlesden-Popper compounds, further indicating that the layering may be harnessed to control the electronic filling of the rare-earth nickelates.

The Ni L_2 spectra presented above are polarization averaged; we now decompose them to compare the x-ray linear dichroic (XLD) signals across the series. At the Ni L edge, we expect from dipole selection rules that only $2p \rightarrow 3d_{3z^2-r^2}$ transitions are allowed for $\mathbf{E}||\mathbf{c}||$ (I_z), and primarily

 $2p \rightarrow 3d_{x^2-y^2}$ transitions are allowed for $\mathbf{E}||\mathbf{a},\mathbf{b}||$ (I_x) [48]. Hence, assuming Nd_2NiO_4 (n = 1) to be in a high-spin state with two half-filled e_g orbitals, we expect a large XLD signal arising from a splitting of the $3d_{3z^2-r^2}$ and $3d_{x^2-v^2}$ orbitals generated by a strong tetragonal distortion [48,49]. In contrast, the dichroism in the NdNiO₃ $(n = \infty)$ film is negligible: with a single half-filled e_g orbital, no dichroism is expected without substantial strain or heterostructure engineering that breaks the double degeneracy of the e_g orbitals [34,61–63]. Thus, the XLD of the mixed-valent n = 2-5 compounds should decrease going from the single-layer Nd₂NiO₄ to the perovskite NdNiO₃. This is indeed the trend observed experimentally in Fig. 3(c). Compressive strain may also contribute to a slight enhancement of this dichroic response. It has been previously shown in nickelate compounds that, in straightening out the NiO_6 octahedra in the c axis and promoting a tetragonal distortion, compressive strain acts to lower the energy of the $3d_{3r^2-r^2}$ orbital and shifts the **E**||**c** spectra to lower energy [63–65]. As we move from the bulk lattice constants of c =3.807 Å in NdNiO₃ $(n = \infty)$ [9] to c = 3.827 Å in Nd₂NiO₄ (n = 1), the compressive strain increases from $\varepsilon \sim -0.45$ to -1%. Hence, our observed trend of an increased XLD signal, with the $3d_{3z^2-r^2}$ (**E**||**c**) peak sitting at lower energy than the $3d_{x^2-y^2}$ (**E**||**a**, **b**), as we decrease the order *n* of the $Nd_{n+1}Ni_nO_{3n+1}$ compounds may also reflect the additional effect of compressive epitaxial strain.

C. Electrical transport

Having demonstrated the structural and electronic modulations of the Ruddlesden-Popper nickelates as a function of layering order n, we now present electrical resistivity measurements for the $Nd_{n+1}Ni_nO_{3n+1}$ for n = 2-5, ∞ in Fig. 4. The n = 1 compound is insulating as in the bulk, likely due to the presence of a charge-stripe-ordered state [6]. The n=2 compound exhibits a near metal-to-insulating transition with minor hysteresis, though we have also observed fully insulating behavior in samples of slightly diminished quality, like observations in bulk La₃Ni₂O₇ [66]. The $n \ge 3$ compounds exhibit a metal-to-insulator transition with a hysteresis reminiscent of the perovskite NdNiO₃, albeit with a far weaker transition to the insulating state. The transition temperatures span between ~87 and 150 K and are generally suppressed with the increasing order of the system, although there is slight variation sample to sample. Intriguingly, both the metal-to-insulator transition temperature and magnitude of the resistivity jump through the transition decrease with the increasing order of the system. This is contrary to an expectation that the resistivities of the $Nd_{n+1}Ni_nO_{3n+1}$, in moving to higher-order n, would begin to approximate those of the parent NdNiO₃ ($n = \infty$).

The bulk $R_4\mathrm{Ni}_3\mathrm{O}_{10}$ compounds possess a second-order metal-to-metal transition at ~ 150 K, emblematic of the formation of a CDW instability [8,37–39]. Interestingly, we do not observe this behavior in our Nd₄Ni₃O₁₀ films stabilized with compressive epitaxial strain, though we have previously found this metal-to-metal transition in thin film Nd₄Ni₃O₁₀ on NdGaO₃ substrates which provide tensile strain [12]. Nevertheless, our compressively strained Nd₄Ni₃O₁₀ films may still possess a CDW transition that is now manifest

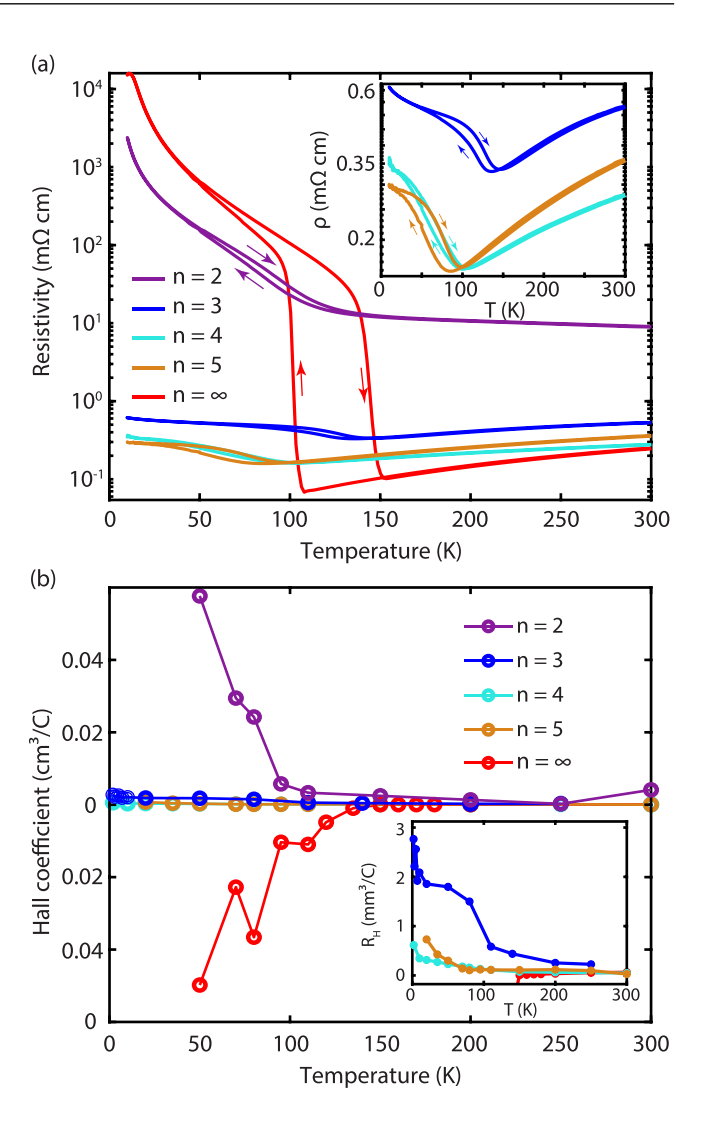


FIG. 4. Electrical characterization of the $Nd_{n+1}Ni_nO_{3n+1}$ thin films. (a) Temperature-dependent resistivity of the $Nd_{n+1}Ni_nO_{3n+1}$ for $n=2-5,\infty$. Arrows indicate the direction of temperature sweeps. The n=1 compound is insulating as in the bulk. Inset is a zoom-in on the n=3-5 compounds. (b) Hall coefficients (R_H) for the $n=2-5,\infty$ compounds. All the Ruddlesden-Popper compounds possess a sudden increase in R_H when cooled through the metal-to-insulator transitions. The R_H behavior for NdNiO₃ ($n=\infty$) exhibits a sign change from positive to negative when cooled into the insulating state. Inset is a zoom-in on the n=3-5 compounds.

as a metal-to-insulator not metal-to-metal transition. The temperature-dependent Hall coefficients exhibit a sharp jump at the transition temperature, as shown in Fig. 4(b). This is consistent with bulk measurements, reflecting a loss of carriers due a Fermi surface reconstruction and CDW instability in $Nd_4Ni_3O_{10}$ [37]. In contrast, the opening of a bond disproportionated gap in the $NdNiO_3$ compounds is reflected in a change in the sign of Hall carriers [67]. Thus, it is likely that the epitaxially stabilized Ruddlesden-Popper compounds still possess a CDW transition as in single-crystal $Nd_4Ni_3O_{10}$ but that compressive epitaxial strain modifies this transition. The precise role of strain on modulating these charge states in these Ruddlesden-Popper compounds would require further investigation. We note that the weak hysteresis and

metal-to-insulator transitions—characteristics which qualitatively resemble the resistivity behavior of NdNiO₃—appear intrinsic to thin film $Nd_{n+1}Ni_nO_{3n+1}$ (n > 3) stabilized on LaAlO₃, as they are reproducible across all high-quality films (see Fig. S5 in the Supplemental Material [27]). These features are likely not due to the presence of trace NdNiO₃, as we do not observe large areas with missing rock salt layers in STEM images, as shown in Fig. 2. Finally, the evolution of the temperature-dependent Hall coefficients in Fig. 4(b) suggest that, as we increase the order of the system, the lowtemperature Hall coefficients decrease, and thus, the bands crossing the Fermi level begin to approximate those in the parent NdNiO₃ [67]. This points to a potential crossover from the incommensurate CDW state in the n = 3 to the fully charge disproportionated state in the $n = \infty$ within the $3 < n < \infty$ range.

IV. CONCLUSIONS

In summary, we have synthesized epitaxial thin films of the neodymium-based Ruddlesden-Popper nickelates $Nd_{n+1}Ni_nO_{3n+1}$ with MBE. Our synthetic strategy carefully optimizes the deposition of the perovskite NdNiO₃ to enable the precise layer-by-layer growth of the Ruddlesden-Popper films and can potentially be generalized to any Ruddlesden-Popper system. XAS at the O K and Ni L edges demonstrate a consistent depletion of the formal nickel $3d^8$ states as we move across the series from n = 1 to ∞ . There is also a concomitant increase in the oxygen character as would be expected from increasing valence [68]. XLD suggests that the splitting between the in-plane and out-of-plane orbitals in the e_g manifold increases, consistent with an increased tetragonal distortion toward n = 1. In the electronic transport, the $n \ge$ 3 compounds exhibit a weakly hysteretic metal-to-insulator transition, though with resistivity changes small compared with the parent NdNiO₃. This resistivity behavior differs from the nonhysteretic, second-order metal-to-metal transitions in bulk $R_{n+1}Ni_nO_{3n+1}$ which are reflective of a CDW instability. The temperature-dependent Hall coefficients, however, suggest that such a CDW-like transition does occur but that this transition begins to cross over to the charge-ordered transition in NdNiO₃ $(n = \infty)$ as n increases. This underscores the apparent sensitivity of these layered nickelates to both epitaxial strain and dimensionality.

Our work invites further exploration of the electronic and magnetic phases in thin film Ruddlesden-Popper systems and proximate to the superconductivity observed in our reduced $Nd_6Ni_5O_{12}$ compound [12]. For example, bulk single-crystal specimens of $Nd_4Ni_3O_{10}$ exhibit intertwined charge and spin density waves [18]. Investigating the coupling of charge and spin order in the layered nickelates would thus be an exciting future pursuit, facilitated by the successful synthesis of thin film Ruddlesden-Popper nickelates. Finally, synthesis of $Nd_{n+1}Ni_nO_{3n+1}$ thin films provides a platform to search for additional superconductivity in the square-planar $Nd_{n+1}Ni_nO_{2n+2}$ compounds.

ACKNOWLEDGMENTS

We thank H. Hijazi at the Rutgers University Laboratory of Surface Modification for assistance in Rutherford backscattering spectrometry. Research is primarily supported by the U.S. Department of Energy (DOE), Office of Basic Energy Sciences, Division of Materials Sciences and Engineering, under Award No. DE-SC0021925. Materials growth was supported by PARADIM under National Science Foundation (NSF) Cooperative Agreement No. DMR-2039380. Electron microscopy was primarily carried out through the use of MIT.nano facilities at the Massachusetts Institute of Technology. Additional electron microscopy and all nanofabrication work was performed at Harvard University's Center for Nanoscale Systems, a member of the National Nanotechnology Coordinated Infrastructure Network, supported by the NSF under Grant No. 2025158. In this paper, we also used resources of the Advanced Light Source, a DOE, Office of Science User Facility under Contract No. DE-AC02-05CH11231. G.A.P. acknowledges support from the Paul & Daisy Soros Fellowship for New Americans and from NSF Graduate Research Fellowship Grant No. DGE-1745303. Q.S. and D.C.C. were supported by the Science and Technology Center for Integrated Quantum Materials, NSF Grant No. DMR-1231319. M.-C.J and A.S.B. acknowledge NSF Grant No. DMR-2045826 and the ASU Research Computing Center for high-performance computing resources. H.E.S. and I.E. were supported by the Rowland Institute at Harvard. E.E.F., B.H.G., and L.F.K. were supported by the NSF (PARADIM) under Cooperative Agreement No. DMR-2039380. J.A.M. acknowledges support from the Packard Foundation and the Gordon and Betty Moore Foundation's EPiQS Initiative, Grant No. GBMF6760.

G.A.P. and Q.S. contributed equally to this paper.

J. B. Torrance, P. Lacorre, A. I. Nazzal, E. J. Ansaldo, and C. Niedermayer, Phys. Rev. B 45, 8209 (1992).

^[2] S. Catalano, M. Gibert, J. Fowlie, J. Iniguez, J.-M. Triscone, and J. Kreisel, Rep. Prog. Phys. 81, 046501 (2018).

^[3] K. Sreedhar, J. M. Honig, M. Darwin, M. McElfresh, P. M. Shand, J. Xu, B. C. Crooker, and J. Spalek, Phys. Rev. B 46, 6382 (1992).

^[4] C. Liu, V. F. C. Humbert, T. M. Bretz-Sullivan, G. Wang, D. Hong, F. Wrobel, J. Zhang, J. D. Hoffman, J. E. Pearson, J. S. Jiang *et al.*, Nat. Commun. 11, 1402 (2020).

^[5] J. Rodriguez-Carvajal, M. Fernandez-Diaz, and J. Martinez, J. Phys.: Condens. Matter 3, 3215 (1991).

^[6] V. J. Emery, S. A. Kivelson, and J. M. Tranquada, Proc. Natl. Acad. Sci. U.S.A. 96, 8814 (1999).

^[7] B. Keimer, S. A. Kivelson, M. R. Norman, S. Uchida, and J. Zaanen, Nature (London) 518, 179 (2015).

^[8] M. Greenblatt, Curr. Opin. Solid State Mater. Sci. 2, 174 (1997).

^[9] P. Lacorre, J. Torrance, J. Pannetier, A. Nazzal, P. Wang, and T. Huang, J. Solid State Chem. **91**, 225 (1991).

^[10] J. Zhang, A. S. Botana, J. W. Freeland, D. Phelan, H. Zheng, V. Pardo, M. R. Norman, and J. F. Mitchell, Nat. Phys. 13, 864 (2017).

^[11] D. Li, K. Lee, B. Y. Wang, M. Osada, S. Crossley, H. R. Lee, Y. Cui, Y. Hikita, and H. Y. Hwang, Nature (London) 572, 624 (2019).

- [12] G. A. Pan, D. Ferenc Segedin, H. LaBollita, Q. Song, E. M. Nica, B. H. Goodge, A. T. Pierce, S. Doyle, S. Novakov, D. Córdova Carrizales *et al.*, Nat. Mater. 21, 160 (2022).
- [13] Z. Zhang and M. Greenblatt, J. Solid State Chem. 117, 236 (1995).
- [14] D.-K. Seo, W. Liang, M.-H. Whangbo, Z. Zhang, and M. Greenblatt, Inorg. Chem. 35, 6396 (1996).
- [15] V. V. Poltavets, K. A. Lokshin, T. Egami, and M. Greenblatt, Mater. Res. Bull. 41, 955 (2006).
- [16] J. Zhang, H. Zheng, Y.-S. Chen, Y. Ren, M. Yonemura, A. Huq, and J. F. Mitchell, Phys. Rev. Materials 4, 083402 (2020).
- [17] H. Li, X. Zhou, T. Nummy, J. Zhang, V. Pardo, W. E. Pickett, J. F. Mitchell, and D. S. Dessau, Nat. Commun. 8, 1 (2017).
- [18] J. Zhang, D. Phelan, A. S. Botana, Y.-S. Chen, H. Zheng, M. Krogstad, S. G. Wang, Y. Qiu, J. A. Rodriguez-Rivera, R. Osborn et al., Nat. Commun. 11, 6003 (2020).
- [19] Z. Li, W. Guo, T. T. Zhang, J. H. Song, T. Y. Gao, Z. B. Gu, and Y. F. Nie, APL Mater. 8, 091112 (2020).
- [20] W. Sun, Y. Li, X. Cai, J. Yang, W. Guo, Z. Gu, Y. Zhu, and Y. Nie, Phys. Rev. B 104, 184518 (2021).
- [21] N. M. Dawley, B. H. Goodge, W. Egger, M. R. Barone, L. F. Kourkoutis, D. J. Keeble, and D. G. Schlom, Appl. Phys. Lett. 117, 062901 (2020).
- [22] C. M. Brooks, L. F. Kourkoutis, T. Heeg, J. Schubert, D. A. Muller, and D. G. Schlom, Appl. Phys. Lett. 94, 162905 (2009).
- [23] M. R. Barone, N. M. Dawley, H. P. Nair, B. H. Goodge, M. E. Holtz, A. Soukiassian, E. E. Fleck, K. Lee, Y. Jia, T. Heeg *et al.*, APL Mater. **9**, 021118 (2021).
- [24] J. Haeni, C. D. Theis, and D. G. Schlom, J. Electroceram. 4, 385
- [25] Y. Li, W. Sun, J. Yang, X. Cai, W. Guo, Z. Gu, Y. Zhu, and Y. Nie, Front. Phys. 9, 443 (2021).
- [26] J. Sun, C. T. Parzyck, J. H. Lee, C. M. Brooks, L. F. Kourkoutis, X. Ke, R. Misra, J. Schubert, F. V. Hensling, M. R. Barone et al., Phys. Rev. Materials 6, 033802 (2022).
- [27] See Supplemental Material at http://link.aps.org/supplemental/ 10.1103/PhysRevMaterials.6.055003 for additional structural and electronic characterization.
- [28] E. Breckenfeld, Z. Chen, A. R. Damodaran, and L. W. Martin, ACS Appl. Mater. Interfaces 6, 22436 (2014).
- [29] D. Preziosi, A. Sander, A. Barthélémy, and M. Bibes, AIP Adv. 7, 015210 (2017).
- [30] I. El Baggari, B. H. Savitzky, A. S. Admasu, J. Kim, S.-W. Cheong, R. Hovden, and L. F. Kourkoutis, Proc. Natl. Acad. Sci. U.S.A. 115, 1445 (2018).
- [31] B. H. Goodge, I. El Baggari, S. S. Hong, Z. Wang, D. G. Schlom, H. Y. Hwang, and L. F. Kourkoutis, Microsc. Microanal. 28, 404 (2022).
- [32] E. E. Fleck, B. H. Goodge, M. R. Barone, H. P. Nair, N. J. Schreiber, N. M. Dawley, D. G. Schlom, and L. F. Kourkoutis, (unpublished).
- [33] W. Wu, D. Huang, G. Guo, H.-J. Lin, T. Hou, C. Chang, C. Chen, A. Fujimori, T. Kimura, H. Huang *et al.*, J. Electron Spectrosc. Relat. Phenom. **137–140**, 641 (2004).
- [34] M. Wu, E. Benckiser, M. W. Haverkort, A. Frano, Y. Lu, U. Nwankwo, S. Brück, P. Audehm, E. Goering, S. Macke *et al.*, Phys. Rev. B 88, 125124 (2013).
- [35] J. B. Nelson and D. P. Riley, Proc. Phys. Soc. 57, 160 (1945).

- [36] B. Burganov, C. Adamo, A. Mulder, M. Uchida, P. D. C. King, J. W. Harter, D. E. Shai, A. S. Gibbs, A. P. Mackenzie, R. Uecker *et al.*, Phys. Rev. Lett. **116**, 197003 (2016).
- [37] Q. Li, C. He, X. Zhu, J. Si, X. Fan, and H.-H. Wen, Sci. China: Phys., Mech. Astron. 64, 227411 (2021).
- [38] B.-Z. Li, C. Wang, P. T. Yang, J. P. Sun, Y.-B. Liu, J. Wu, Z. Ren, J.-G. Cheng, G.-M. Zhang, and G.-H. Cao, Phys. Rev. B 101, 195142 (2020).
- [39] D. Rout, S. R. Mudi, M. Hoffmann, S. Spachmann, R. Klingeler, and S. Singh, Phys. Rev. B 102, 195144 (2020).
- [40] T. H. Kim, T. R. Paudel, R. J. Green, K. Song, H.-S. Lee, S.-Y. Choi, J. Irwin, B. Noesges, L. J. Brillson, M. S. Rzchowski et al., Phys. Rev. B 101, 121105(R) (2020).
- [41] C.-H. Lee, N. D. Orloff, T. Birol, Y. Zhu, V. Goian, E. Rocas, R. Haislmaier, E. Vlahos, J. A. Mundy, L. F. Kourkoutis et al., Nature (London) 502, 532 (2013).
- [42] J. H. Lee, G. Luo, I. C. Tung, S. H. Chang, Z. Luo, M. Malshe, M. Gadre, A. Bhattacharya, S. M. Nakhmanson *et al.*, Nat. Mater. 13, 879 (2014).
- [43] Y. Nie, Y. Zhu, C.-H. Lee, L. F. Kourkoutis, J. A. Mundy, J. Junquera, P. Ghosez, D. Baek, S. Sung, X. Xi et al., Nat. Commun. 5, 4530 (2014).
- [44] H. P. Nair, J. P. Ruf, N. J. Schreiber, L. Miao, M. L. Grandon, D. J. Baek, B. H. Goodge, J. P. C. Ruff, L. F. Kourkoutis, K. M. Shen et al., APL Mater. 6, 101108 (2018).
- [45] F. M. F. de Groot, M. Grioni, J. C. Fuggle, J. Ghijsen, G. A. Sawatzky, and H. Petersen, Phys. Rev. B 40, 5715 (1989).
- [46] J. Suntivich, W. T. Hong, Y.-L. Lee, J. M. Rondinelli, W. Yang, J. B. Goodenough, B. Dabrowski, J. W. Freeland, and Y. Shao-Horn, J. Phys. Chem. C 118, 1856 (2014).
- [47] P. Kuiper, J. van Elp, G. A. Sawatzky, A. Fujimori, S. Hosoya, and D. M. de Leeuw, Phys. Rev. B 44, 4570 (1991).
- [48] E. Pellegrin, J. Zaanen, H.-J. Lin, G. Meigs, C. T. Chen, G. H. Ho, H. Eisaki, and S. Uchida, Phys. Rev. B 53, 10667 (1996).
- [49] P. Kuiper, J. van Elp, D. E. Rice, D. J. Buttrey, H.-J. Lin, and C. T. Chen, Phys. Rev. B 57, 1552 (1998).
- [50] T. Mizokawa, D. I. Khomskii, and G. A. Sawatzky, Phys. Rev. B 61, 11263 (2000).
- [51] V. Bisogni, S. Catalano, R. J. Green, M. Gibert, R. Scherwitzl, Y. Huang, V. N. Strocov, P. Zubko, S. Balandeh, J.-M. Triscone et al., Nat. Commun. 7, 13017 (2016).
- [52] Z. Hu, M. S. Golden, J. Fink, G. Kaindl, S. A. Warda, D. Reinen, P. Mahadevan, and D. D. Sarma, Phys. Rev. B 61, 3739 (2000).
- [53] S. Kunisada, S. Isono, Y. Kohama, S. Sakai, C. Bareille, S. Sakuragi, R. Noguchi, K. Kurokawa, K. Kuroda, Y. Ishida et al., Science 369, 833 (2020).
- [54] P. Di Pietro, M. Golalikhani, K. Wijesekara, S. K. Chaluvadi, P. Orgiani, X. Xi, S. Lupi, and A. Perucchi, ACS Appl. Mater. Interfaces 13, 6813 (2021).
- [55] J. Fink, Th. Müller-Heinzerling, B. Scheerer, W. Speier, F. U. Hillebrecht, J. C. Fuggle, J. Zaanen, and G. A. Sawatzky, Phys. Rev. B 32, 4899 (1985).
- [56] J. W. Freeland, M. van Veenendaal, and J. Chakhalian, J. Electron Spectrosc. Relat. Phenom. **208**, 56 (2016).
- [57] I-Cheng Tung, G. Luo, J. H. Lee, S. H. Chang, J. Moyer, H. Hong, M. J. Bedzyk, H. Zhou, D. Morgan, D. D. Fong *et al.*, Phys. Rev. Materials 1, 053404 (2017).
- [58] L. F. Kourkoutis, H. Xin, T. Higuchi, Y. Hotta, J. Lee, Y. Hikita, D. Schlom, H. Hwang, and D. Muller, Philos. Mag. 90, 4731 (2010).

- [59] J. A. Mundy, Y. Hikita, T. Hidaka, T. Yajima, T. Higuchi, H. Y. Hwang, D. A. Muller, and L. F. Kourkoutis, Nat. Commun. 5, 3464 (2014).
- [60] C. Piamonteze, F. M. F. de Groot, H. C. N. Tolentino, A. Y. Ramos, N. E. Massa, J. A. Alonso, and M. J. Martínez-Lope, Phys. Rev. B 71, 020406(R) (2005).
- [61] J. Chaloupka and G. Khaliullin, Phys. Rev. Lett. 100, 016404 (2008).
- [62] A. S. Disa, D. P. Kumah, A. Malashevich, H. Chen, D. A. Arena, E. D. Specht, S. Ismail-Beigi, F. J. Walker, and C. H. Ahn, Phys. Rev. Lett. 114, 026801 (2015).
- [63] A. S. Disa, F. Walker, S. Ismail-Beigi, and C. H. Ahn, APL Mater. 3, 062303 (2015).

- [64] J. Freeland, J. Liu, M. Kareev, B. Gray, J. Kim, P. Ryan, R. Pentcheva, and J. Chakhalian, Europhys. Lett. 96, 57004 (2011).
- [65] I. C. Tung, P. V. Balachandran, J. Liu, B. A. Gray, E. A. Karapetrova, J. H. Lee, J. Chakhalian, M. J. Bedzyk, J. M. Rondinelli, and J. W. Freeland, Phys. Rev. B 88, 205112 (2013).
- [66] Z. Zhang, M. Greenblatt, and J. Goodenough, J. Solid State Chem. 108, 402 (1994).
- [67] A. J. Hauser, E. Mikheev, N. E. Moreno, T. A. Cain, J. Hwang, J. Y. Zhang, and S. Stemmer, Appl. Phys. Lett. 103, 182105 (2013).
- [68] J. Zaanen, G. A. Sawatzky, and J. W. Allen, Phys. Rev. Lett. 55, 418 (1985).